# THE RADIAL DISTRIBUTION OF X-RAY BINARIES AND GLOBULAR CLUSTERS IN NGC 4649 AND THEIR RELATION WITH THE LOCAL STELLAR MASS DENSITY

S. Mineo[1,2], G. Fabbiano[1], R. D'Abrusco[1], T. Fragos[1], D.-W. Kim[1], J. Strader[3],
J. P. Brodie[4], J. S. Gallagher[5], A. Zezas[6], and B. Luo[5,7]

[1] Harvard-Smithsonian Center for Astrophysics, 60 Garden Street Cambridge, MA 02138, USA; smineo@head.cfa.harvard.edu
[2] Department of Physics, University of Durham, South Road, Durham DH1 3LE, UK
[3] Department of Physics and Astronomy, Michigan State University, East Lansing, MI 48824, USA
[4] UCO/Lick Observatory, 1156 High Street, Santa Cruz, CA 95064, USA
[5] Department of Astronomy, University of Wisconsin, Madison, WI 53706-1582, USA
[6] Physics Department, University of Crete, P.O. Box 2208, GR-710 03, Heraklion, Crete, Greece
[7] Department of Astronomy & Astrophysics, 525 Davey Lab, The Pennsylvania State University, University Park, PA 16802, USA

## ABSTRACT

We investigate the radial distribution of the low-mass X-ray binary (LMXB) population in the elliptical galaxy NGC 4649, using *Chandra* and *Hubble* data to separate the field and globular cluster (GC) populations. GCs with LMXBs have the same radial distribution as the parent red and blue GCs. The radial profile of field LMXBs follows the *V*-band profile within the *D*25 of NGC 4649. Using the spatial information provided by our data, we find that the global galaxy-wide relations among cumulative number and luminosity of LMXBs and the integrated stellar mass hold on *local* scales within *D*25. An excess of field LMXBs with respect to the *V*-band light is observed in the galaxy's outskirts, which may be partially due to unidentified GC sources or to a rejuvenated field LMXB population caused by past merging interactions.

*Key words:* binaries: general – galaxies: individual (NGC 4946/NGC 4947) – galaxies: interactions – X-rays: binaries

*Online-only material:* color figures

## 1. INTRODUCTION

Given the old age of the stellar populations of elliptical galaxies, there is no doubt that the X-ray-emitting accretion binaries detected in copious numbers in these galaxies with *Chandra* (see the review by Fabbiano 2006) are low-mass X-ray binaries (LMXBs), with sub-solar companion stars. These LMXB samples have rekindled the discussion on the origin of LMXBs that began with their discovery in the Milky Way (see Giacconi 1974). *Chandra* observations show that LMXBs are found both in globular clusters (GCs) and in the stellar field. Dynamical formation in GCs is the most efficient way to form LMXBs, which could then disperse in the field because of formation kicks or evaporation of the parent cluster (Clark 1975; Grindlay et al. 1984; Kundu et al. 2002, 2007; Bildsten & Deloye 2004). While less efficient, the evolution of a native binary in the stellar field is also a viable LMXB formation channel (Verbunt & van den Heuvel 1995). Both mechanisms are likely to take place in elliptical galaxies, since their LMXB content depends on both the total stellar mass of the galaxy and its GC specific frequency (Kim & Fabbiano 2004; Gilfanov 2004). Moreover, at the lower luminosities ($L_X < 10^{37}$ erg s$^{-1}$), the X-ray luminosity functions (XLFs) of GC and field LMXBs clearly differ, suggesting different families of sources (Voss & Gilfanov 2007; Voss et al. 2009; Kim et al. 2009; Zhang et al. 2011).

Not all GCs are similarly effective at forming LMXBs. Several factors may affect the probability of dynamical LMXB formation. One factor is the stellar encounter rate, which is a function of the GC mass and compactness/radius (Verbunt & Lewin 2006; Sivakoff et al. 2007; Jordán et al. 2007; Peacock et al. 2010). The galactocentric radius has also been noted, in the sense that more centrally located GCs have been reported in

some cases to be more likely to host LMXBs; however, this also may be a byproduct of the stellar encounter rate, since centrally located GCs may also be more compact (Hodge 1962; van den Bergh et al. 1991; Brodie & Strader 2006; Masters et al. 2010; Fabbiano et al. 2010). Finally, most GC LMXBs reside within red, metal-rich GCs (Grindlay 1993; Bellazzini et al. 1995; Kundu et al. 2007, 2002; Maccarone et al. 2004; Jordán et al. 2004; Kim et al. 2006; Sivakoff et al. 2007). The metallicity effect is the strongest, as demonstrated by a recent study by Kim et al. (2013) making use of all the available *Chandra* and *Hubble Space Telescope* (*HST*) data, which also finds that the ratio of GC LMXB fractions in metal-rich to metal-poor GCs is $3.4 \pm 0.5$ for a wide range of X-ray luminosities. Ivanova et al. (2012) suggest that these differences can be explained by the increase in number densities and average masses of red giants in higher metallicity populations, where red giants operate as seeds for LMXB dynamical formation.

While the bulk of the above conclusions on LMXB formation in elliptical galaxies has been reached based on the study of the XLFs (and global content of LMXBs), the spatial distribution of LMXBs may offer different important clues. The results so far are contradictory. In particular, some authors concluded that overall the LMXB distribution follow closely the stellar light (Kim & Fabbiano 2003; Humphrey & Buote 2004; Kim et al. 2006) and comparisons of the radial distributions of field and GC LMXBs in a few galaxies did not reveal significant differences (Sarazin et al. 2003; Jordán et al. 2004; Kim et al. 2006), but these studies may have been affected by poor statistics as well as by heterogeneous selection of GCs from *HST* and ground-based (KPNO 4 m) observations. Kundu et al. (2007) instead concluded that GC and field LMXBs follow different distributions, therefore suggesting that field LMXBs should be formed in the stellar field. Based on overall galaxy properties,
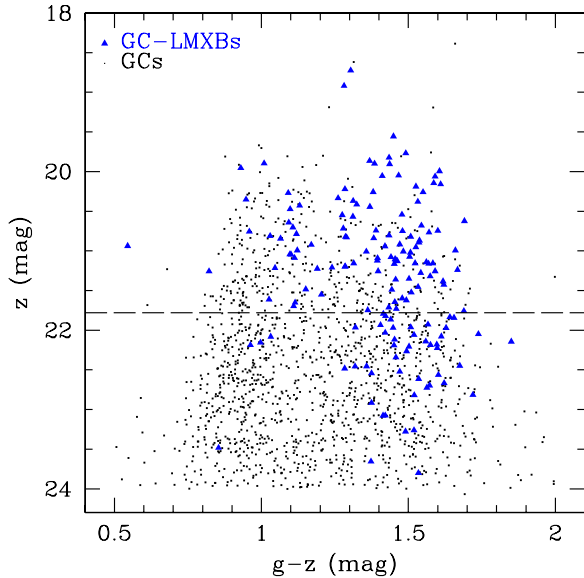
**Figure 1.** $z$ vs. $g-z$ color–magnitude diagram of GCs in NGC 4649. The black points are all GCs from Strader et al. (2012) sample (1603 sources). The blue triangles are those (157) matched with the X-ray sources from Luo et al. (2013) catalog (see Section 3.2 for details). The horizontal dashed line indicates the >90% completeness level for ground-based data (see Section 3.3 for details), for comparison with *HST* data.

(A color version of this figure is available in the online journal.)

Irwin (2005) and Juett (2005) argued for in situ formation of field LMXBs, while Kim et al. (2009) suggested the possibility of a mixed origin (see also Irwin 2005).

Our large coverage with both *Chandra* and *HST* of the Virgo elliptical NGC 4649 (Strader et al. 2012; Luo et al. 2013) enables us to revisit this question, with a rich population of several hundreds LMXBs and a homogeneous and complete GC population. The present work is based on the X-ray source catalog of the elliptical galaxy NGC 4649 by Luo et al. (2013) and the associated optical catalog of GCs detected with *HST* by Strader et al. (2012). We adopt a distance to NGC 4649 of 16.5 Mpc. In Section 2, we discuss our data samples; in Section 3, we analyze the radial distribution of GCs (both red and blue) and their associated LMXBs; we derive the radial distributions of field LMXBs and compare them with those of GC LMXBs, GCs, and stellar light, which is a proxy of the integrated stellar mass. In Section 4, we discuss our results. Our main conclusions are summarized in Section 5.

## 2. DATA

The data are from our full-coverage joint *Chandra–HST* survey of NGC 4649 (P.I.: Fabbiano). The original samples comprise 1603 GCs (Strader et al. 2012) and 501 X-ray sources (Luo et al. 2013). From these samples, we excluded all sources detected within the $D25$ ellipse of the nearby spiral galaxy NGC 4647 and those within the central ($R < 0\farcs17$) region of NGC 4649; the latter step avoids confusion. We thus obtained 1516 GCs, of which 731 are blue, $(g-z) < 1.18$, and 785 are red, $(g-z) \gtrsim 1.18$ ($g$ and $z$ are both AB magnitudes). These GCs and the associated 157 X-ray sources are plotted in the $z$ versus $(g-z)$ space in Figure 1. As expected (see Fabbiano 2006, and references therein), most X-ray sources are hosted by red and luminous GCs. The samples used in this work are summarized in Table 1.

**Table 1**
Summary of the Data

| | GCs | | | X-ray Sources | | | |
| --- | --- | --- | --- | --- | --- | --- | --- |
| | Red | Blue | Tot | Red GCs | Blue GCs | Field | Tot |
| All | 785 | 731 | 1516 | 128 | 29 | 268 | 425 |
| Complete | 329 | 297 | 626 | 59 | 18 | 151 | 228 |
| AGN-subtracted | . . . | . . . | . . . | 59 | 18 | 120 | 197 |

**Note.** Blue: $(g-z) < 1.18$, red: $(g-z) \gtrsim 1.18$, X-ray completeness limit $L_{\mathrm{lim}} = 4.8 \times 10^{37}$ erg s$^{-1}$, optical GC completeness limit: $z < 22.2$ mag.

There are 280 X-ray sources with no GCs counterpart, of which 74 reside outside the *HST* survey area. To establish if some of these sources are associated with GCs, we matched their positions with the GCs in the catalog of Lee et al. (2008). The latter, from KPNO 4 m telescope images, reach to a projected radius of $\sim 8\farcm2$ and are >90% complete to $T_1 \sim 23$ ($V \sim 22.5$). We excluded the resulting 12 GC matches from the field LMXBs sub-sample and converted their $(C - T_1)$ colors into $(g - z)$ in order to separate blue and red GCs. All of them are associated with luminous GC candidates, for which contamination effects are low. For comparison with *HST* data, we converted the value of $V$ discussed above into $z$, using the equation $V = 0.753 \times (g - z) - 0.108 + z$ (C. Usher 2013, in preparation), assuming an average $(g - z) = 1.1$. We show the >90% completeness level for ground-based data in Figure 1, which suggests that a fraction of low-luminosity GCs, and therefore their GC LMXBs, may still remain undetected in the ground-based data.

For uniformity and sensitivity, only GCs and GC LMXBs from the *HST* sample were used for the data analysis throughout the paper. Using the $z$-band completeness curves from Jordán et al. (2009) for the typical GC half-light radius $r = 0\farcs0385$, the GC sample is complete for $z < 22.2$ mag at all radial bins of our grid. However, when comparing two distributions equally affected by incompleteness, we include faint GCs to maximize statistics; these cases will be specified at their occurrence.

We adopted a common threshold luminosity for the X-ray sources, at $4.8 \times 10^{37}$ erg s$^{-1}$, corresponding to 50% completeness at the $11^{\mathrm{th}}$ radial bin ($5\farcm0$–$5\farcm5$ from the galaxy center, enclosing the $D25$ ellipse). We corrected the radial distribution of field LMXBs using the spatially resolved completeness function $K(L)$ of Luo et al. (2013). Throughout this paper, we account for the contribution of background active galactic nuclei (AGNs) to the X-ray source counts in the field, both in terms of number and luminosity, using the $\log N - \log S$ determined by Georgakakis et al. (2008). This correction is not needed for GC LMXBs, thanks to the matches with GCs.

## 3. RADIAL DISTRIBUTIONS OF X-RAY SOURCES AND GCs

To construct the radial distribution of X-ray sources and GCs, we used the grid of circular annuli from Luo et al. (2013), which is matched to the spatially resolved completeness function $K(L)$ of the same authors (see their Figure 3). The annuli are centered in the center of NGC 4649 and extend from a radius $R = 0\farcs17$ out to a radius $R = 7\farcm5$ with constant linear spacing of $0\farcs5$.

### 3.1. Globular Clusters

The radial profiles of the red and blue GCs are presented in Figure 2. Red GCs are more centrally concentrated than
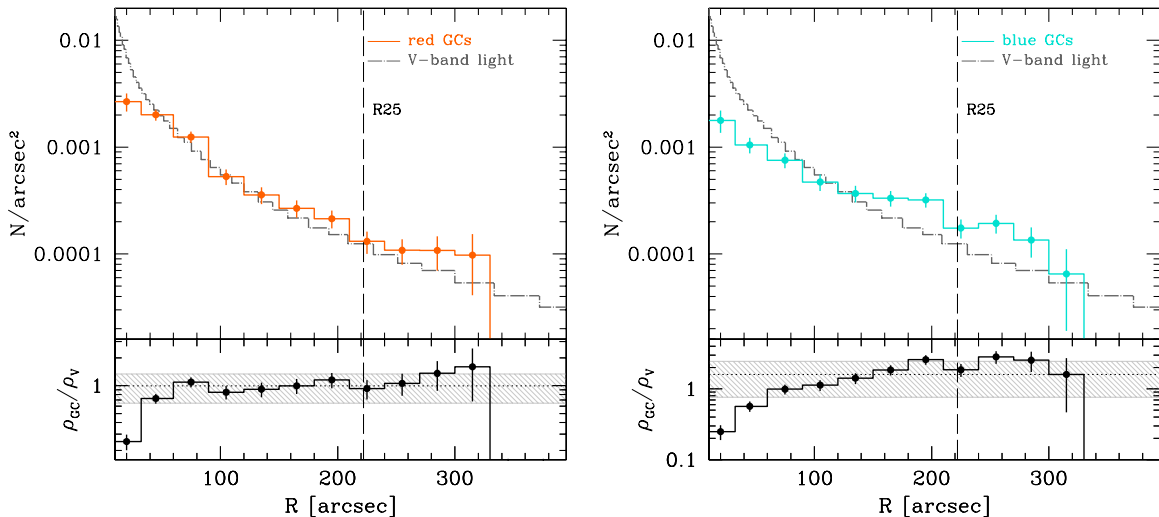
**Figure 2.** Comparison between the radial distribution of red GCs (left panel, solid orange line) and blue GCs (right panel, solid cyan line) with the radial distribution of the $V$-band light (dashed gray line). To compare the distribution of GCs with the $V$-band radial profile, we plot the complete GC sample ($z < 22.2$ mag; see Section 3.2). Error bars are $1\sigma$ uncertainties assuming a Poisson distribution. The $V$-band radial profile, in both panels, was renormalized as in Figure 4 to facilitate comparisons. Both GC profiles were renormalized to the mean $\rho_{\rm GCs}/\rho_V$ ratio for red GCs between $\sim 50''$ and $\sim 200''$, which is rather flat. In the bottom panel of each figure, we plot the ratio between the number of GCs and the mean value of the $V$-band light at the given radial bin. The horizontal dotted line shows the average value of the $N_{\rm GCs}$-to-$V$-band light ratio within the radial bins covered with both GCs detections and $V$-band light. The shaded region indicates the $1\sigma$ standard deviation of the mean. The X-ray sources within the $D25$ region of the nearby spiral galaxy NGC 4647 were excluded and the area of circular annuli were corrected accordingly.

(A color version of this figure is available in the online journal.)

blue GCs and follow more closely the distribution of the stellar surface brightness, with the exception of a flattening at the inner radii ($R \lesssim 40''$). This is typical of GC populations (see, e.g., Brodie & Strader 2006, and references therein; see also Figure 5 of Strader et al. 2012).

We compared the radial distribution of GCs sources with the composite radial profile of the $V$-band light of Kormendy et al. (2009). The $V$-band profile was constructed from many different data sources (see Table 2 in Kormendy et al. 2009) and is in Vega magnitudes. We plot the complete GCs sample having $z < 22.2$ mag. The $\rho_{\rm GCs}/\rho_V$ ratio curves (bottom panel of Figure 2) show that the profile of red GCs seems to be fairly consistent, between $\sim 40''$ and $\sim 200''$, with the $V$-band light and therefore with the stellar mass of the host galaxy (see Section 3.4 below), although the ratio over the entire range could also be consistent with a slow increasing gradient. In contrast, the distribution of blue GCs does not follow the $V$-band profile, except for radii between $30''$ and $120''$ with the adopted normalization.

### 3.2. LMXBs in GCs

In Figure 3, we compare the radial profiles of the red and blue GCs with the associated LMXBs. In this case, no $z$-band magnitude cut was applied to the GCs, to maximize the number of GC LMXBs. The incompleteness correction was instead applied to the distributions of X-ray sources. In the bottom of each panel, we show the ratio between the number density of GCs and GC-associated X-ray sources ($\rho_{\rm GCs}/\rho_X$) in each radial bin, along with their uncertainties. These ratios are uniform in the area of good *Chandra* and *HST* spatial coverage, meaning that on average the population of GCs with LMXBs has the same radial distribution as the parent red and blue GC distributions, as in NGC 1399 (Paolillo et al. 2011). A Kolmogorov–Smirnov (KS) test yields $D$ values for red and blue GCs of $D_{\rm red} = 0.25$, $D_{\rm blue} = 0.28$, giving two-sided KS statistics probabilities of 0.91 and 0.77, respectively. This indicates that the distributions are likely drawn from

same underlying distributions. We have verified that the optical incompleteness does not affect the conclusion above, although it slightly changes the mean $\rho_{\rm GCs}/\rho_X$ values since LMXBs are generally found in bright GCs. It also worsens the statistics of LMXBs at each radial bin, which results in larger error bars.

### 3.3. LMXBs in the Field

To construct the radial distribution of field LMXBs, we only used sources above the X-ray completeness limit and applied the X-ray incompleteness corrections. We calculated the area underlying the radial bins by taking into account the X-ray exposure map coverage as well as by subtracting the area corresponding to the $D25$ ellipse of the nearby spiral galaxy NGC 4647. Based on the corrected areas, we subtracted the predicted contribution of background AGNs at each bin and converted the resulting number into number density.

The resulting surface density of field LMXBs is compared with the $V$-band radial profile in the left panel of Figure 4. The uncertainties include the $1\sigma$ Poisson errors on the number of sources and both Poisson and 20% uncertainty from cosmic variance on the expected AGN number per bin (see Section 5.1 in Luo et al. 2012, and references therein). We see a clear agreement between the observed radial profile for field LMXBs and the $V$-band profile, within the $D25$ of NGC 4649; the KS test yields $D_{\rm field} = 0.31$ and a two-sided KS statistics probability of 0.56. At $D25$, the data are suggestive of a possible dip. The face value of the statistical significance for the lack of sources, based on the $V$-band profile between $R25$ and $320''$, is $3.3\sigma$. However, this could be binning-related and should not be considered as a firm statistical conclusion. Using different binning, we would lose information about the X-ray incompleteness, therefore we are not able to test the source dip further. Looking at both panels of Figure 4, it is evident that the gap in the field LMXB profile would be filled by the GC LMXBs, suggesting that the lack of sources is not due to systematics. The KS statistics probability after we include the data outside the $D25$ ellipse drops to 0.09. At a radius of $\sim 400''$, a moderately significant ($\approx 2\sigma$) excess of
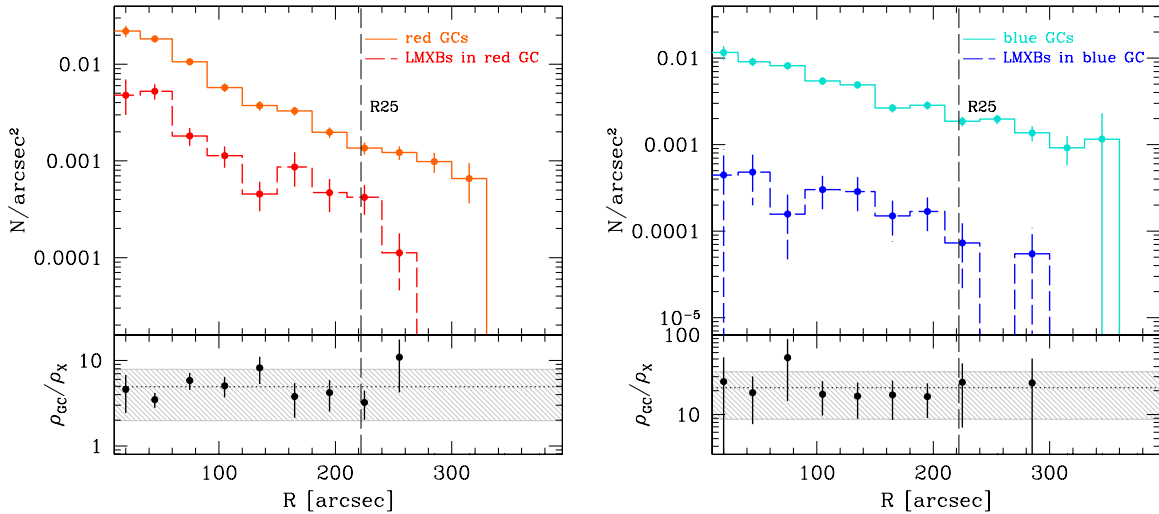
**Figure 3.** Same as Figure 2, but we did not apply a *z*-band magnitude cut. Also plotted are the distributions of LMXBs detected in red (left, dashed red line) and blue (right, dashed blue line) GCs. Note that the effects of GC incompleteness in the *z* band are the same for the two (GC and LMXB) distributions. The X-ray incompleteness correction was also applied on the distributions of X-ray sources. In the bottom panel of each figure, we plot the ratio between the number densities of GC and X-ray sources ($\rho_{GCs}/\rho_X$) in each radial bin. The horizontal dotted line shows the mean value of the $\rho_{GCs}$-to-$\rho_X$ ratio within the first 10 radial bins, i.e., in the region where both the X-ray sources and GCs were detected. The shaded region indicates the $1\sigma$ standard deviation of the mean.

(A color version of this figure is available in the online journal.)
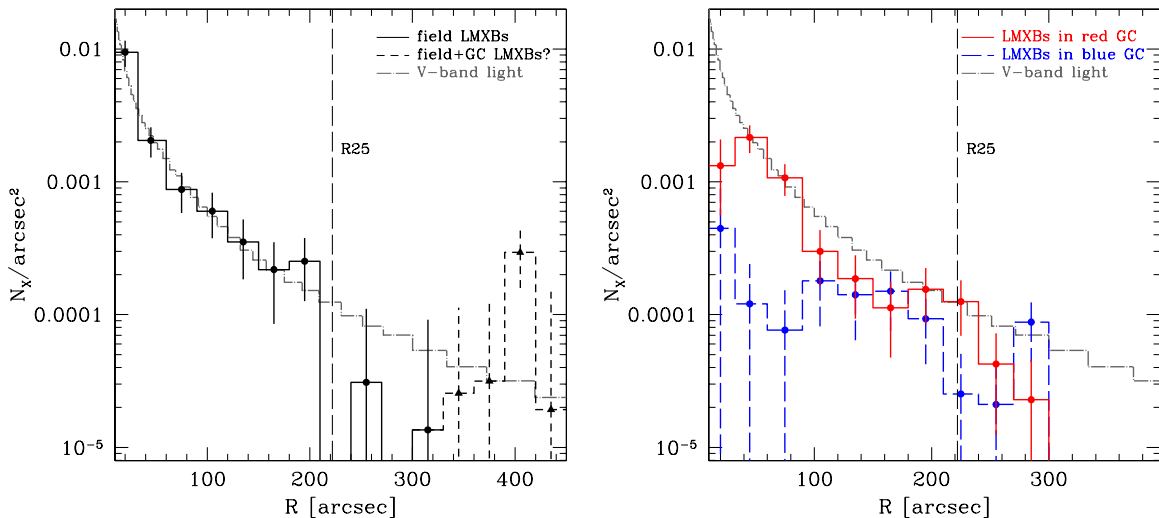


**Figure 4.** Same as Figure 2, but for the field LMXBs (left) and LMXBs in red/blue GCs (right) with both X-ray and optical incompleteness effects corrected (see Sections 3.1 and 3.2 for details). For $R \gtrsim 320''$, there are no optical data on GCs, therefore the field profile might be contaminated by GC LMXBs and it is marked with a dashed line and black filled triangles. The contribution of background AGNs per bin was subtracted only from the number of field LMXBs. This correction was not necessary for the GC LMXBs due to the GC association itself. The 20% uncertainty on the background AGN number per bin is included in the error calculation. The *V*-band radial profile, in both panels, was renormalized in order to match the first bin of the profile for field LMXBs. The same normalization was used in Figure 2.

(A color version of this figure is available in the online journal.)

LMXBs with respect to the *V*-band light is observed. However, some of these "field" LMXBs may be associated with GCs, for which we lack optical coverage (Section 2). In Figure 4, we mark these outer LMXBs with a different line.

### 3.4. Comparison of LMXBs in GCs with Field LMXBs

For a comparison of the radial distribution of GC LMXBs with field LMXBs, the incompleteness in both GC and X-ray samples was taken into account (Table 1). To the GC sources, we added the 12 matches with the GCs in the catalog of Lee et al. (2008; Section 2).

The resulting radial distributions are shown in the right panel of Figure 4, compared with the *V*-band light. As expected, LMXBs are preferentially found in red GCs, which also seem

to follow the *V*-band light profile, within the statistics, except for the centermost bin. Considering only the *HST* sample, we find that red GCs contain 3.3 times more LMXBs than blue GCs (Table 1), as already reported for this galaxy in Kim et al. (2013).

## 4. DISCUSSION

### 4.1. LMXBs and Stellar Mass

Gilfanov (2004) showed that the number of LMXBs in old stellar populations scales with the stellar mass. Kim & Fabbiano (2004) reached the same conclusion, while also showing a dependence on the specific frequency of GCs (i.e., the number of GCs per unit mass) of each galaxy. The agreement between
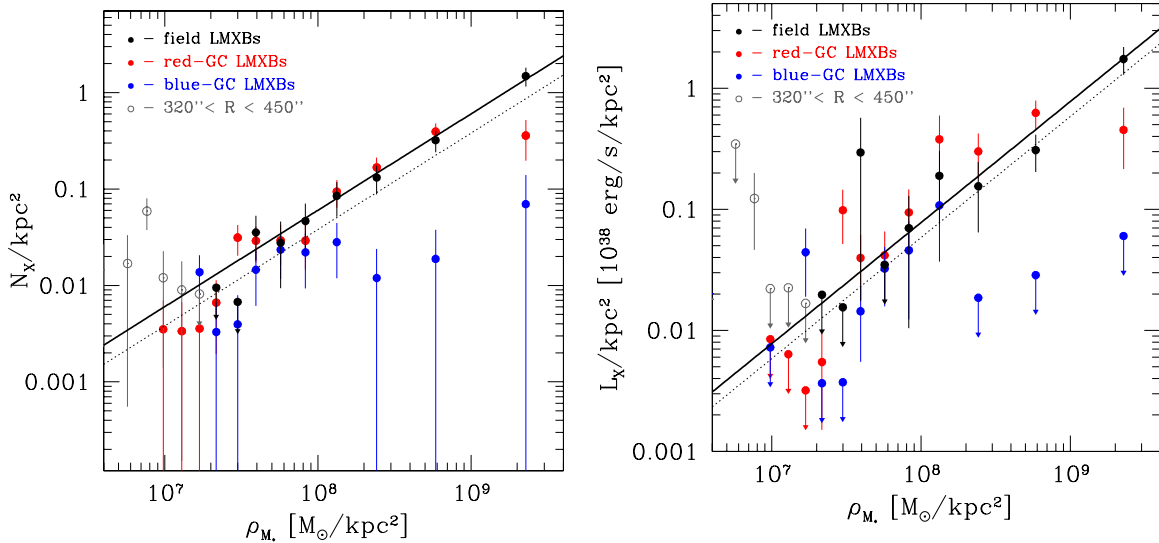
**Figure 5.** Relation between the *local* stellar mass density in NGC 4649 ($M_\odot$ kpc$^{-2}$), the number density ($N_X$/kpc$^2$, left panel), and luminosity density ($L_X$/kpc$^2$, right panel) of LMXBs in the field (black filled circles) and in GCs (red and blue filled circles). The data were obtained using the *V*-band profile. Field sources at radii $R > 320''$ may be contaminated by GC LMXBs (see Section 4) and therefore are marked with different symbols (gray empty circles). In all panels, we plot the best-fitting linear relation (solid lines) for field LMXBs obtained using only the *V*-band profile and the galaxy-wide average relations (dotted lines) from Gilfanov (2004).

(A color version of this figure is available in the online journal.)

**Table 2**
Summary of the Parameters for the $N_X$/kpc$^2$–$\rho_{M_\star}$, $L_X$/kpc$^2$–$\rho_{M_\star}$
Relations Obtained from the $\chi^2$ Fit

| Relation | Free Slope | | | Linear Fit | |
|---|---|---|---|---|---|
| | $\log K$ | $\beta$ | $\chi^2$/dof | $\log K$ | $\chi^2$/dof |
| | | Field LMXBs | | | |
| $N_X$/kpc$^2$–$\rho_{M_\star}$ | $-9.29 \pm 0.80$ | $1.01 \pm 0.09$ | 1.52/7 | $-9.22 \pm 0.05$ | 1.53/8 |
| $L_X$/kpc$^2$–$\rho_{M_\star}$ | $-7.46 \pm 1.27$ | $0.81 \pm 0.14$ | 6.80/5 | $-9.11 \pm 0.08$ | 8.49/6 |

**Notes.** The parameters are relative to the field LMXB data fitted with power-law models $\log(N_X/\text{kpc}^2, L_X/\text{kpc}^2) = \log K + \beta \log(\rho_{M_\star})$, where $L_X$ is in units of $10^{38}$ erg s$^{-1}$, using the $\chi^2$ minimization technique, setting the slope $\beta$ free and fixing it to unity, respectively. The error on both the slope and $K$ were computed with the standard $\Delta\chi^2 = 1$ prescription. See Section 4 for details.

field LMXBs and the *V* band shows that this mass dependence of the LMXB population is uniform locally in NGC 4649, at least within *D*25.

In Appendix A.2, we derive a map of the stellar mass, which we compare with the *V*-band profile to obtain the mass conversion. The resulting number and luminosity density/mass plots are shown in Figure 5. The best-fitting power law, obtained via $\chi^2$ minimization for the number density/mass field LMXB sample is linear; the luminosity density/mass relation may be slightly flatter (Figure 5 and Table 2). We excluded the points at $R > 320''$ from these fits because of the lack of *HST* coverage (see Section 2). Within the uncertainties of the two relations, our best fit is consistent with Gilfanov (2004).

However, the Gilfanov (2004) scaling relation was calibrated on the entire LMXB populations in nearby galaxies, with no separation between field and GC LMXBs. If we include GC LMXBs, we obtain a 3.3 times larger scaling factor than Gilfanov (2004). This discrepancy may be due to the high GC specific frequency of NGC 4649 ($S_N = 3.8 \pm 0.4$; Lee et al. 2008, $S_N = 5.16 \pm 1.20$; Peng et al. 2008), which is also important for the normalization of the LMXB luminosity functions (Kim & Fabbiano 2004). A further source

of discrepancy between our calibration and that by Gilfanov (2004) may be related to the methods for mass estimates. Gilfanov (2004) obtained the stellar mass for each galaxy through the calibration by Bell & de Jong (2001). Our stellar mass is based on the calibration by Zibetti et al. (2009). According to Zibetti et al. (2009), there are minor systematic effects on mass estimates induced by different choices of initial mass function (IMF) (Salpeter IMF in Bell & de Jong 2001; Chabrier (2003) IMF in Zibetti et al. 2009), since the IMF can be considered uniform within a galaxy. More relevant discrepancies may be introduced by the assumption of other parameters, such as star formation history, metallicity, and dust, which are expected to vary significantly from place to place within a galaxy.

Comparing our results with the $L_X$–$M_\star$ relation from Gilfanov (2004), we found a larger normalization by a factor of 2.7, consistent with the $N_X$–$M_\star$ discrepancy.

### 4.2. LMXB Populations in Red and Blue GCs

The distribution of LMXBs in blue GCs is uncorrelated with the stellar mass of the host galaxy and clearly differs from that of red GC LMXBs, which follow the stellar mass distribution of the host galaxy except for the inner region ($R < 30''$; $\rho \gtrsim 2 \times 10^9 M_\odot$ kpc$^{-2}$). Comparing the innermost bin of $\rho_{M_\star}$ in Figure 5 with the best-fitting $N_X$/kpc$^2$–$\rho_{M_\star}$ and $L_X$/kpc$^2$–$\rho_{M_\star}$ relations for field LMXBs, we find that both the number and luminosity densities of LMXBs in red GCs significantly deviate from the best-fitting linear model for field LMXBs ($6\sigma$ and $5.6\sigma$, respectively). A similar deficit is seen comparing the red GC population with the *V*-band light. This deficit is well known and it is thought to be due to preferential destruction of GCs near the center.

Figure 5 suggests also that in the region of $\rho_{M_\star}$ between $10^8$ and $10^9 M_\odot$ kpc$^{-2}$, the distribution of red GC LMXBs in the $L_X$/kpc$^2$–$\rho_{M_\star}$ plane is skewed toward slightly higher luminosities if compared with field LMXBs. This difference cannot be due to the observed difference between the XLFs

of GC and field LMXBs (Kim et al. 2009) because the latter becomes significant at $L_X < 5 \times 10^{37}$ erg s$^{-1}$, below our completeness limit.

We find 3.3 times more LMXBs in red than blue GCs (Table 1). This ratio is typical for elliptical galaxies (see, e.g., Fabbiano 2006) and is in good agreement with previous results (Sarazin et al. 2003; Jordán et al. 2004; Kim et al. 2006, 2009; Kundu et al. 2007; Sivakoff et al. 2007). Kim et al. (2013) demonstrated that this ratio is found at all LMXB luminosities. Ivanova (2006) proposed that metallicity-dependent magnetic braking with main sequence donors may explain the observed difference, but this only works at lower luminosities ($<2 \times 10^{37}$ erg s$^{-1}$). To explain the metallicity effect of luminous neutron star (NS) LMXBs, Ivanova et al. (2012) further proposed that red giants serve as seeds for the dynamical production of bright LMXBs and the increase of the number densities and masses of red giants boosts the LMXB production for both white dwarf and red giant donors.

The number fraction of GC LMXBs, i.e., the ratio of the number of GC LMXBs (in both red and blue GCs) and the total number of LMXBs in both field and GCs, is ∼40%, in agreement with the findings of Kim et al. (2009) based on deep *Chandra* observations of the three elliptical galaxies NGC 3379, NGC 4278, and NGC 4696. However, the total fraction of GCs hosting an LMXB with $L_X \gtrsim 4.8 \times 10^{37}$ erg s$^{-1}$, is ∼12% (77 out of 626), a factor of ∼2 larger than that found by Kim et al. (2009). In particular, ∼18% of red GCs (59 out of 329) and ∼6% of blue GCs (18 out of 297) host an LMXB brighter than $4.8 \times 10^{37}$ erg s$^{-1}$. This inconsistency may be related to the extraordinarily luminous XLF of NGC 4649 (Sarazin et al. 2003; Randall et al. 2004).

### 4.3. GC Specific Frequency and LMXB Formation

White et al. (2002) first noted a correlation between the abundance of LMXBs in early-type galaxies and the GC specific frequency $S_N$, consistent with a part of the overall LMXB population at least being of GC origin. These results, however, could not address the question of the origin of the field LMXBs: in situ or GC formation (e.g., Grindlay et al. 1984; Verbunt & van den Heuvel 1995; Bildsten & Deloye 2004). Irwin (2005) and Juett (2005) explored this relation to conclude that the field LMXB population is likely formed in situ. Kim et al. (2009) and Paolillo et al. (2011) pursued these comparisons further by using the GC and field LMXBs identified in four nearby galaxies. To these, we can now add NGC 4649 (Figure 6). Note that the values used in the present work are different than those of the original publications. For consistency, they are calculated using the same luminosity threshold as for NGC 4649 (our completeness limit $4.8 \times 10^{37}$ erg s$^{-1}$). For this galaxy, we calculated the number of field and GC LMXBs within the $D25$ and normalized them for the $K$-band luminosity. In computing both the X-ray source numbers and the galaxy's $K$-band luminosity, we excluded the central region as well as the $D25$ region of NGC 4647. We keep in mind that the higher $L_X$ limit reduced more field LMXBs than GC LMXBs, because of the flattening of the GC LMXB XLF (Voss et al. 2009; Kim et al. 2009). We adopted the $S_N$ estimate from the ground-based data by Lee et al. (2008), $3.8 \pm 0.4$. We conclude that overall the linear relation between $N_X/L_K$ and $S_N$ is stronger in GC LMXBs than in field LMXBs, as suggested by Kim et al. (2009), although the scatter is large. The presence of a (weaker) dependence of the field LMXB number density
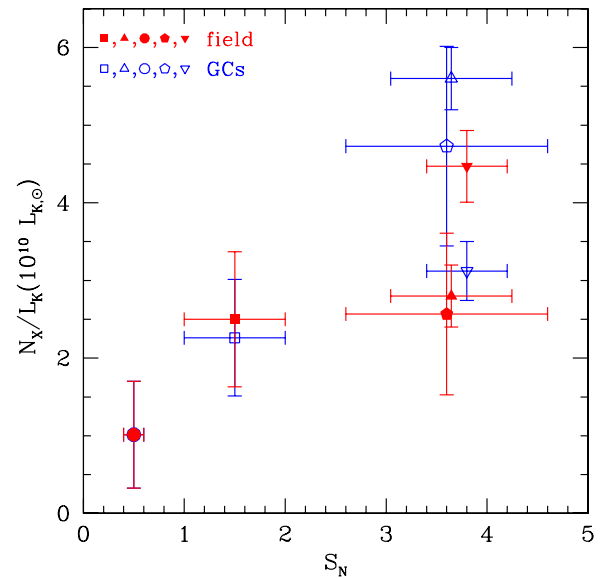


**Figure 6.** Number of field LMXBs (filled symbols) and GC LMXBs (open symbols) brighter than $4.8 \times 10^{37}$ erg s$^{-1}$ vs. GC specific frequency $S_N$. The symbols represent NGC 3379 (circles), NGC 4697 (squares), and NGC 4278 (pentagons) from Kim et al. (2009), NGC 1399 (straight triangles) from Paolillo et al. (2011), and NGC 4649 (upside down triangles). For NGC 4946, we used the $S_N$ estimate from Lee et al. (2008), $3.8 \pm 0.4$.

(A color version of this figure is available in the online journal.)

on $S_N$ is consistent with a partial contribution of LMXBs that originated in GCs to the native field LMXB population.

### 4.4. Census of Bright LMXBs in NGC 4649

Three ultra-luminous X-ray sources (ULXs) are detected in the field. This number is in agreement with the 2.4 sources predicted by the background AGNs $\log N - \log S$ (Georgakakis et al. 2008) above $10^{39}$ erg s$^{-1}$.

One ULX is associated with a red GC (also in this case in agreement with the predicted number of background AGNs). The latter has $L_X \approx 2.14 \times 10^{39}$ erg s$^{-1}$ and is the source CXOU J124346.9+113234 identified and analyzed in depth by Roberts et al. (2012). These authors concluded that this object is a good candidate to be a black hole radiating at super-Eddington luminosities, although they did not exclude the possibility that this is a highly super-Eddington NS. There is no evidence of ULXs in blue GCs. We searched for the source identification using the SIMBAD[8] astronomical database. We note that the counterparts are all within $0\farcs8$ from the detected X-ray source, which corresponds to the 99% uncertainty circle of *Chandra* absolute positions for sources within $3'$ of the aimpoint. Among the bright sources detected in the field, one is identified as X-ray source, one as X-ray binary, and one as a quasi-stellar object (quasar) by Pineau et al. (2011) and Wu & Jia (2010). The first two sources are most likely ULXs. The results reported in the present section are summarized in Table 3.

### 4.5. LMXBs in the Galaxy's Outskirts

As discussed in Section 3.3, the radial profile of field LMXBs departs from the $V$-band light (stellar mass) profile outside $D25$ of NGC 4649, first suggesting a relative lack of LMXBs and then showing a possible excess at larger radii. The latter at face value would be consistent with similar peripheral overdensities

---

8 http://simbad.u-strasbg.fr/simbad/

**Table 3**
Ultra-luminous X-Ray Sources ($L_X \geqslant 10^{39}$ erg s$^{-1}$) in NGC 4649

| $\alpha_{J2000}$ (h:m:s) | $\delta_{J2000}$ (d:m:s) | $L_X$ (erg s$^{-1}$) | Loc | ID | Separ (arcsec) |
|---|---|---|---|---|---|
| (1) | (2) | (3) | (4) | (5) | (6) |
| 12:43:32.22 | 11:39:50.0 | $1.32 \times 10^{39}$ | Field | X | 0.8 |
| 12:43:36.53 | 11:30:09.4 | $5.5 \times 10^{39}$ | Field | XB | 0.4 |
| 12:43:46.91 | 11:32:34.1 | $2.14 \times 10^{39}$ | Red GC | XB | 0.2 |
| 12:44:08.94 | 11:33:33.3 | $4.9 \times 10^{39}$ | Field | Q | 0.8 |

**Notes.** (1) Right ascension (J2000); (2) declination (J2000); (3) 0.5–8 keV luminosity in erg s$^{-1}$; (4) location (field/GC); (5) identification: X = X-ray binary source, XB = X-ray binary, identifications by Pineau et al. (2011); Q= quasi-stellar object, identification by Pineau et al. (2011) and Wu & Jia (2010); (6) separation of the identified counterpart from the detected X-ray source. See Section 4.4 for details.

reported by Zhang et al. (2012) in a sample of early-type galaxies, which included NGC 4649. Zhang et al. (2012) ascribed this flattening to both blue GCs and to formation kicks of sources connected with the stellar population at relatively smaller galactocentric radii. In our case, the shape of the radial profile past $D25$ and, in particular, the "dip", is hard to reconcile with the formation kick hypothesis, which would generate a general flattening of the source distribution. GC contamination at large radii of the field LMXB sample is possible because of the lack of deep GC data at those radii (see Section 2). The relatively higher average luminosity of the field LMXB sample at these outer radii, suggested by the flatter-than-linear luminosity–density/mass distribution (Table 2), would be consistent with this hypothesis, given the possible over-luminosity of GC LMXBs relative to those in the field (see Figure 5 and Section 4.2).

An alternate possibility is that of a rejuvenation of the field LMXB population of NGC 4649 at large radii, caused by tidal encounters or accretion of companion or satellite galaxies. Such an interaction may be presently beginning with NGC 4647 (Lanz et al. 2013). This scenario is also suggested by the anisotropy we find in the two-dimensional distribution of GCs and LMXBs in NGC 4649 at large radii (R. D'Abrusco et al. 2013, in preparation). Population synthesis models of native field binary evolution suggest that the X-ray luminosity of these sources (per unit stellar mass) would evolve with age—younger sources would be relatively more luminous (Fragos et al. 2013b, 2013a). This effect is not expected for GC sources (Ivanova et al. 2008; Zhang et al. 2012)

Taking the predictions by Fragos et al. (2013a) at face value, an increase by a factor of ∼2.7 in $L_X/M_\star$ compared with the value reported by Gilfanov (2004) suggests that the younger population in the outskirts of NGC 4649 has a mean stellar age of approximately $4 \pm 1$ Gyr.

## 5. SUMMARY AND CONCLUSIONS

We have reported a large-area study of the LMXB and GC populations of NGC 4649. We find that:

1. The LMXBs in the field follow the stellar mass distribution of the host galaxy within the $D25$ ellipse, but depart from it at larger radii.
2. The LMXBs in red GCs follow a radial distribution consistent with that of their parent red GCs. This distribution is consistent with the $V$-band light and therefore with the stellar mass of the host galaxy, except for the higher density

region at $R < 40''$, $\rho_{M_\star} \gtrsim 6 \times 10^8 \, M_\odot$ kpc$^{-2}$, where they show a significant (>3.5σ) underdensity if compared with field LMXBs.

3. LMXBs in blue GCs, on average, have the same radial distribution as their parent blue GCs, which is uncorrelated with the stellar mass of the host galaxy.
4. Comparing NGC 4649 with other four early-type galaxies for which similar quality data are available, we find that the LMXB population of NGC 4649 is consistent with a stronger dependence of the number of sources with the GC specific frequency for the GC LMXBs than field LMXBs, although a weaker trend persists in the field LMXBs.

Our results are consistent with a prevalent in situ origin for the field LMXBs, although with some contamination from LMXBs dynamically formed in red GCs. The deviations at outer radii of the LMXB radial profile from that of the stellar mass density may be in part due to contamination by GC LMXBs, given our lack of GC coverage at these outer radii. The shape of the radial profile is not consistent with the hypothesis that these outer sources may be the result of formation kick displacements only (Zhang et al. 2012). We speculate that a rejuvenation of the field LMXB population (Fragos et al. 2013b, 2013a) at larger radii, connected with tidal interactions and/or galaxy mergers, may be responsible for the excess high-luminosity sources in these regions.

## APPENDIX A

### STELLAR MASS SURFACE BRIGHTNESS MAP

Stellar mass is the most important parameter in the investigation of gas-poor galaxies. In the last decade, several studies have proven the existence of a tight correlation between the collective number of LMXBs and the integrated stellar mass of the

host early-type galaxies and bulges of late-type galaxies (e.g., Kim & Fabbiano 2004; Gilfanov 2004). This relation can now be explored in greater detail, using spatially resolved maps of stellar mass surface density that can be constructed based on optical and near-infrared (NIR) images, following the prescription from Zibetti et al. (2009).

The fiducial method from Zibetti et al. (2009) results from a careful comparison between stellar population synthesis models and multiband images. They use images from both Two Micron All Sky Survey (2MASS) and the Sloan Digital Sky Survey (SDSS) to express the stellar mass-to-light ratio ($M/L$) as a function of the $H$-band (1.66 $\mu$m) light and the ($g - i$) and ($i - H$) colors (where the $g$ and $i$ bands have effective wavelengths of 475 nm and 763 nm, respectively). The two sets of images have reasonably similar resolutions (2″.5 and 1″.3 FWHM, respectively). The resulting stellar mass surface density maps have a typical accuracy of <30% at any pixel.

According to the same authors, in early-type galaxies, which lack young stellar populations, a good approximation of their method can be obtained using only one color, ($g - i$). We adopted this recipe to construct the spatially resolved stellar mass distribution in NGC 4649. Following the results of Zibetti et al. (2009) summarized in their Table B, and based on the power-law fits to the $M/L$ as a function of one color, the stellar mass at each pixel $j$, in units of $M_\odot$, was estimated as follows:

$$\Sigma_{M_\star, j} = \Sigma_{H, j} \Upsilon_{H, j}(g - i), \qquad (A1)$$

where $\Sigma_{H, j}$ is the $H$-band surface brightness and $\Upsilon_{H, j}(g - i) = 10^{-1.222 + 0.780(g - i)_j}$.

We used background-subtracted images of NGC 4649 in the $H$ band from the 2MASS Large Galaxy Atlas[9] and in the $g$ and $i$ bands from the SDSS-III[10] public archive. The SDSS images are mosaics of "corrected frames," which are calibrated and sky subtracted. As the pixel scales of the 2MASS and SDSS images are different (1″ pixel$^{-1}$ and 0″.396 pixel$^{-1}$, respectively), we have degraded the SDSS $g$- and $i$-band images in order to match the resolution of the 2MASS $H$-band image. This was done using the routine HASTROM from the NASA IDL Astronomy User's Library,[11] which properly interpolates without adding spatial information.

Due to the typical low signal-to-noise ratio (S/N) of the SDSS images, we adaptively smoothed the $g$- and $i$-band images before transforming them into maps of magnitude per pixel. We only applied slight smoothing in order to overcome the S/N degradation at outer radii. We used ADAPTSMOOTH[12], a code developed by Zibetti et al. (2009) that enhances the S/N with a minimum loss of effective resolution and by keeping the photometric fluxes unaltered. We ran ADAPTSMOOTH for individual SDSS maps requiring an S/N >3 per pixel and a maximum smoothing radius of 10 pixels. We set a background-dominated noise mode and used the background rms in the two bands as input. The latter was measured by means of the MMM routine from NASA's IDL Astronomy User's Library. Along with each smoothed image, we obtained a mask that contains the smoothing radius for each pixel. The two masks were combined into a common mask having the maximum of the two smoothing radii at each pixel. In order to match the spatial resolution between the two bands, we ran the adaptive smoothing again

on the original $g$- and $i$-band maps using the common mask as input. We required the same S/N threshold as before, but the smoothing radius at each position was provided in the input mask. The new $g$- and $i$-band maps were converted into maps of magnitude per pixel in the respective bands. The ($g - i$) color map was obtained by subtracting the $i$ mag from the $g$ mag at each pixel.

The $H$-band image was left in its original resolution. Its pixel values were converted into luminosities in solar units, assuming solar $H$-band magnitude of 3.32 mag (Binney & Merrifield 1998) and a distance to NGC 4649 of 16.5 Mpc.

The maps of $H$-band surface brightness and $M/L$ were finally combined following Equation (A1) to obtain the final image of stellar mass surface density with the same pixel coordinates as the 2MASS $H$-band image. A more elaborate version of this map, where heavier adaptive smoothing was applied for more qualitative purposes, is shown in Figure 7. Figure 8 shows the color map in units of ($g - i$), obtained by combining SDSS $g$- and $i$-band images. Note the difference between the young stellar population in NGC 4647 and the old stellar population in NGC 4649.

### A.1. Comparison with NIR and Optical light Distributions

We performed a qualitative check on the stellar mass distribution resulting from the map obtained in the previous section. We extracted the stellar mass radial profile using the same set of 15 concentric circular annuli defined in Luo et al. (2013; see Section 3 for details). The stellar mass radial profile within the $D25$ ellipse of NGC 4649, in units of $M_\odot$ arcmin$^{-2}$, is shown in Figure 9 (left panel, solid, black line). Using the same set of radial bins, we constructed the radial profile of the light in the $K_S$ band (2.16 $\mu$m). We renormalized the latter in order to give the same value as the stellar mass profile in the first radial bin. We plot the radial profile of the $K_S$-band light in Figure 9 (left panel) with a red dashed line and we note that it is consistent with the profile of stellar mass.

To check the effects of the S/N degradation of 2MASS and SDSS images at outer radii on the stellar mass distribution, we plot in the same figure the surface brightness of the $V$-band magnitude (blue, dash-dotted line) provided by Kormendy et al. (2009) in a number of radial bins larger than those used for the stellar mass and $K_S$ profiles. This profile is in units of mag arcsec$^{-2}$ and extends out to $R \sim 11$'.5 from the center of NGC 4649. We converted it into units of Jy arcsec$^{-2}$ by assuming $F_0 = 3640$ Jy as flux at $m_V = 0$. The average of the values of the $V$-band profile within 0″.17–0″.5 (the first radial bin) was used to renormalize it in order to match the stellar mass profile at the same bin.

From the left panel of Figure 9, it is evident that the three profiles are in good agreement out to a radius of ∼150″. At larger radii, both the stellar mass and the $K_S$ distributions start decreasing more steeply than the $V$-band profile. This is likely due to the effects of the S/N degradation of 2MASS and SDSS images. The difference between the stellar mass and the $K_S$ profiles at ∼200″ is due to the slightly smoothed ($g - i$) color map included in the stellar mass profile. The agreement of the two profiles at smaller radii confirms that the $H$-band light is the main driver of the stellar mass distribution along the galaxy (see Appendix A).

Based on the considerations above, the stellar mass surface brightness map will be used for further analysis (see, e.g., Section 4) only within a radius of ∼150″ from the center of NGC 4649. At larger radii, we will instead use the $V$-band radial

---

[9] http://irsa.ipac.caltech.edu/applications/2MASS/LGA/
[10] http://www.sdss3.org/index.php
[11] http://idlastro.gsfc.nasa.gov/
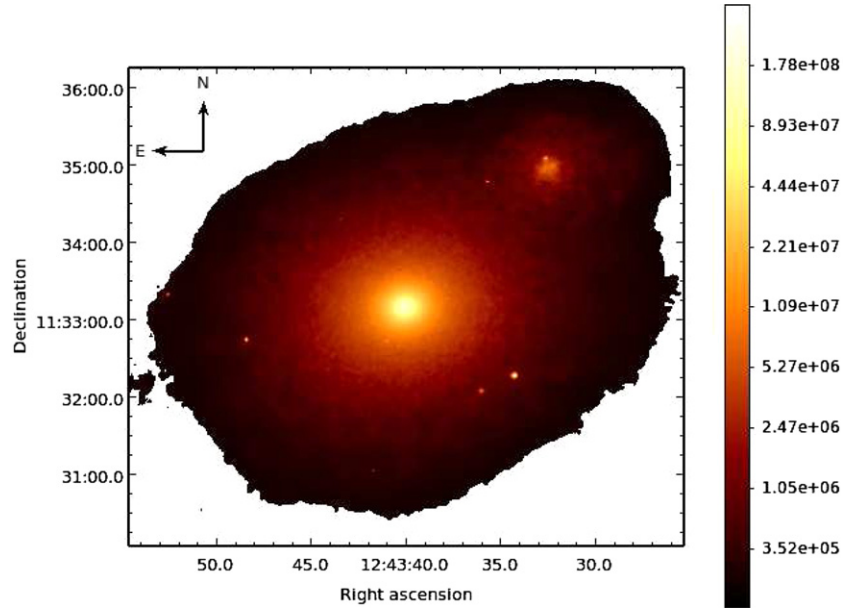[12] http://www.arcetri.astro.it/~zibetti/Software/ADAPTSMOOTH.html

**Figure 7.** Stellar mass surface brightness map for NGC 4649 and NGC 4647, in units of $M_\odot$, obtained by combining 2MASS $H$-band and SDSS $g$- and $i$-band images according the prescription from Zibetti et al. (2009). The map has the same pixel coordinates as the 2MASS $H$-band image. See Appendix A for details. The spiral galaxy NGC 4647, approximately $2'.5$ away from NGC 4649, is also shown in the stellar mass image, although we excluded it from the analysis.

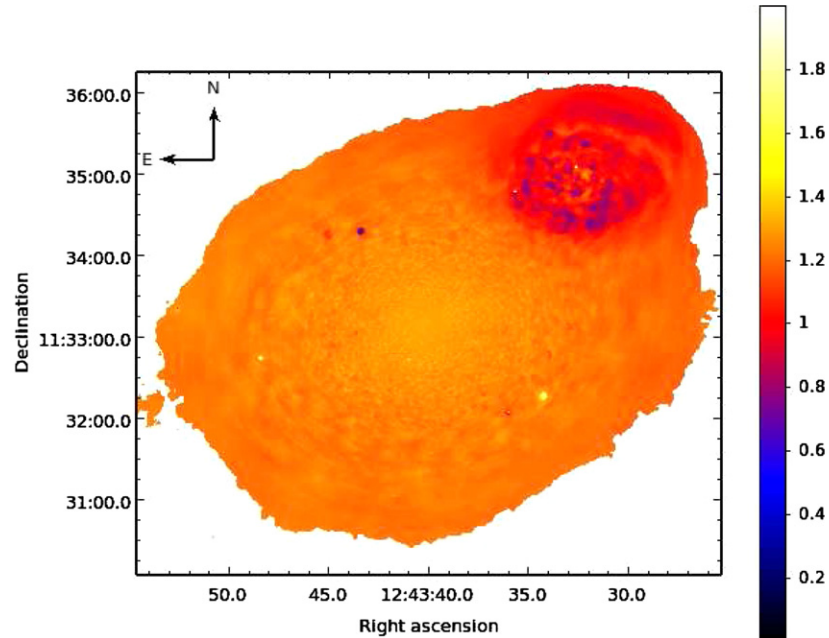(A color version of this figure is available in the online journal.)



**Figure 8.** Color map for NGC 4649 and NGC 4647, in units of $(g - i)$, obtained by combining SDSS $g$- and $i$-band images.
(A color version of this figure is available in the online journal.)

profile (see Sections 3 and 4). We adopt the latter as standard profile at outer radii because it is a composite profile, carefully constructed from as many data as possible (see Kormendy et al. 2009, for details).

### A.2. Derivation of the Spatially Resolved $N_X$–$M_\star$, $L_X$–$M_\star$ Relations Using the Stellar Mass Map

We started from the stellar mass surface brightness image obtained as described in Appendix A. We use the stellar mass density map within a radius of $\sim 150''$ ($\sim 2'.5$) from the center NGC 4649, where the stellar mass radial profile is in good

agreement with the $V$-band radial profile (see Appendix A.1 for details). The few bright spots in the mass surface density map are most likely foreground stars and were masked out. We also masked the $D25$ region of NGC 4647 and the circle at the center of NGC 4649 with radius $R = 0'.17$. The stellar mass surface brightness image $\Sigma_{M_\star}$, constructed in units of $M_\odot$, was transformed into a stellar mass *density* map $\rho_{M_\star}$, in units of $M_\odot\,\mathrm{kpc}^{-2}$.

A set of stellar mass density bins, with constant logarithmic spacing, was defined. The X-ray source number and their collective luminosity were assigned to each bin of stellar mass
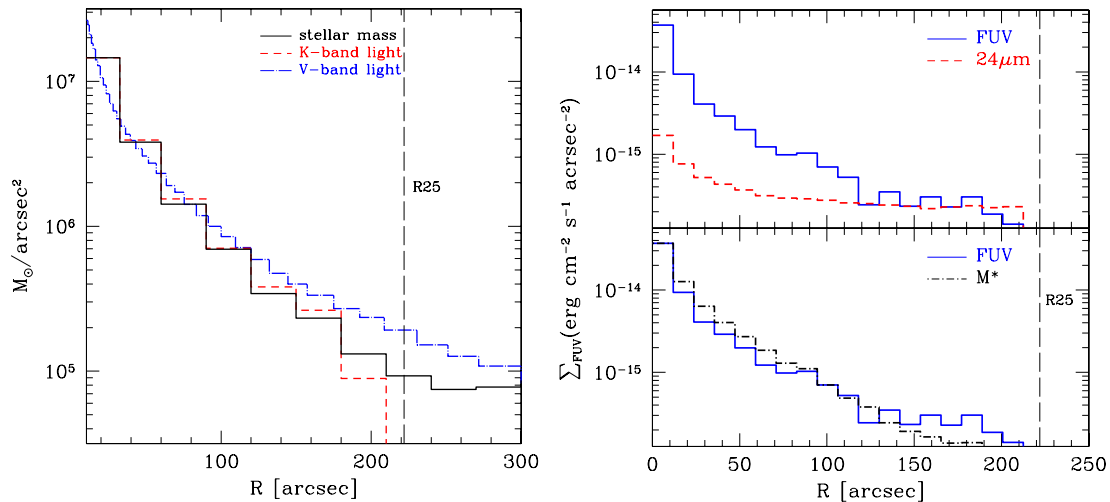
**Figure 9.** Left: the radial profile of the stellar mass (solid black line) within the $D25$ ellipse of NGC 4649, in units of $M_\odot$ arcmin$^{-2}$. The stellar mass distribution was obtained by combining 2MASS $H$-band and SDSS $g$- and $i$-band images (see Appendix A for details). For comparison, we also plot the $K_S$-band light (dashed red line) from 2MASS archival data and the $V$-band radial profile (dash-dotted blue line) from Kormendy et al. (2009). These two curves are renormalized in order to match the first bin of the stellar mass distribution. The semi-major axis of the $D25$ ellipse is shown with a dashed vertical line. Upper-right panel: the radial distributions of far-infrared and far-ultraviolet light in NGC 4649. For a qualitative comparison between the two, we renormalized the far-infrared radial profile in order to match the far-ultraviolet profile at the bin of lowest surface brightness. The far-infrared distribution appears to be flatter and less extended than the far-ultraviolet distribution. Lower-right panel: the radial distributions of stellar light, $M_\star$ (see Appendix A), and far-ultraviolet light in NGC 4649. The stellar light was renormalized in order to match the first bin of the far-ultraviolet surface density. As expected (O'Connell 1999), the two profiles seem to match along the galaxy extent. The semi-major axis of the $D25$ ellipse is shown with a dashed vertical line.

(A color version of this figure is available in the online journal.)

density according to the stellar mass density value at the position of the X-ray source. We selected sources whose X-ray luminosity exceeds $4.8 \times 10^{37}$ erg s$^{-1}$, the same threshold as used to construct the profiles of field and GC-associated LMXBs (see Section 3). The number and luminosity of field and GC LMXBs per stellar mass density bin were then corrected for the effects of incompleteness, following the same procedure as described in Section 3.3. From the incompleteness-corrected number and luminosity of field LMXBs per bin of stellar mass density, we subtracted the predicted contribution of background AGNs at a given bin. We counted the number of pixels in each bin of stellar mass density and their cumulative area. Knowing the area, based on the log $N$–log $S$ function from Georgakakis et al. (2008), we calculated the predicted number of background AGNs and their luminosity above the same threshold luminosity, as discussed above. The resulting number and luminosity of field LMXBs were divided by the total area in kpc$^2$ in each bin. In constructing the analogous distributions for LMXBs associated with red and blue GCs, we did not apply the correction for background AGNs because of the GC association itself. As we compare the distributions of LMXBs in red and blue GCs, the optical incompleteness was not taken into account as its effects are the same for the two distributions. The error bars in both number and luminosity densities at each bin of stellar mass density were computed by taking into account the Poisson noise in the incompleteness-corrected number of sources detected in the bin.

The pixel-by-pixel analysis of the stellar mass density map described above could not be performed at large radii ($R > 150''$) due to noise in the SDSS images. As the SDSS-based stellar mass profile and $V$-band profile seem to agree well in the central area ($R < 150''$) and do not show any features at large radii (see Appendix A), we derived the $V$-band mass-to-light ratio and computed the mass density from the $V$-band profile in the outer regions.

The final values of surface density of X-ray point sources ($N_X$/kpc$^2$) and luminosity ($L_X$/kpc$^2$, in units of $10^{38}$ erg s$^{-1}$ kpc$^{-2}$) are plotted against the value of the stellar mass surface density in Figure 5. Along with the data, in Figure 5 we show the best-fitting linear $N_X$/kpc$^2$–$\rho_{M_\star}$ and $L_X$/kpc$^2$–$\rho_{M_\star}$ relations obtained below.

## APPENDIX B

## INFRARED AND ULTRAVIOLET LIGHT DISTRIBUTIONS

The far-infrared (FIR) and ultraviolet (UV) light from galaxies provides a wide range of information on the properties of their stellar populations and are observed, with different morphological properties, in both late-type and early-type galaxies. The FIR emission originates from dust grains heated by ionizing UV photons, which can be produced by the photospheres of both young and old stars.

In this section, we discuss the FIR and UV emission in both the elliptical galaxy NGC 4649 and the spiral galaxy NGC 4647. We use publicly available *Galaxy Evolution Explorer* (*GALEX*) far-ultraviolet (FUV, 1529 Å) and near-ultraviolet (NUV, 2312 Å) background-subtracted images from the All Sky Surveys program[13] and *Spitzer* MIPS 24 $\mu$m Large Field image ("post basic calibrated data" products)[14]. The 24 $\mu$m background was measured in a region away from the galaxies and subtracted from the NGC 4649 and NGC 4647 emissions.

We report the detection of a bright infrared point source in the MIPS 24 $\mu$m field at ~36$''$ northeast from the center of NGC 4649. We attempted to identify the source, bearing in mind that the point spread function of the MIPS 24 $\mu$m images is ~6$.''$0 FWHM. We first searched for foreground sources

---

[13] http://galex.stsci.edu/GR4/?page=mastform
[14] http://irsa.ipac.caltech.edu/applications/Spitzer/Spitzer/

using the Naval Observatory Merged Astrometric Dataset[15] (Zacharias et al. 2004). This catalog is a merger of data from the *Hipparcos*, Tycho-2, UCAC-2, and USNO-B1 catalogs, supplemented by photometric information from the 2MASS final release point source catalog. The closest source found is at $\sim 26''$ S–W from the infrared source. A search in the SIMBAD database[16] reveals the presence of a red, $(g - z) \sim 1.5$, GC, $190.9202879 + 11.5441650$, reported by Jordán et al. (2009), at a distance of only $4''.8$ southeast from the infrared source. However, as we are unable to safely determine the nature of the aforementioned bright infrared source, we decided to mask it and exclude it from the analysis of the FIR emission from NGC 4649.

### B.1. FIR and FUV Light Distributions for NGC 4649

The $24\,\mu$m emission from elliptical galaxies is thought to be produced by circumstellar outflows of dust-rich gas from old, mass-losing, red giant stars by illumination from their photospheres (see, e.g., Temi et al. 2007, 2008, and references therein). This is confirmed by the evidence of a tight linear correlation between the luminosity at $24\,\mu$m and the $K_S$-band luminosity in elliptical galaxies (e.g., Temi et al. 2009).

Similarly, the FUV radiation in elliptical galaxies is smoothly distributed. It follows the optical light from old stellar populations. In particular, old, metal-rich, low-mass stars that are in the helium-burning phase of the horizontal branch are thought to produce the FUV radiation (see O'Connell 1999, for an extensive review). This makes the FUV emission in early-type galaxies a tracer of the stellar mass loss. The contributions from active nuclei and from a minority of massive stars in a old population are not important in most cases. The latter can be due to recent star formation events in elliptical galaxies associated with massive cluster cooling flows.

The radial distributions of FIR and FUV light in NGC 4649 are shown in the upper-right panel of Figure 9. For a qualitative comparison between the two, we renormalized the FIR radial profile in order to match the FUV profile at the bin of lowest surface brightness. The FIR distribution appears to be flatter than that of the FUV, suggesting that the hot horizontal branch stars may have lost nearly all of their envelopes, therefore we may see only residual $24\,\mu$m emission that is weaker than the FUV (O'Connell 1999).

In the lower-right panel of Figure 9, we compare the FUV profile with the stellar mass distribution, obtained in Appendix A. We have renormalized the latter in order to match the first bin of the FUV surface density. The two profiles seem to be consistent along the galaxy extent, confirming the scenario discussed above. For a more quantitative comparison, we used the correlation between the luminosity at $24\,\mu$m and the $K_S$-band luminosity from Temi et al. (2009). We measured the integrated $24\,\mu$m luminosity within the $D25$ region of NGC 4649 (from which the contribution from NGC 4647 was removed) and obtained $L_{24\mu m} = 1.4 \times 10^{42}$ erg s$^{-1}$. Given this luminosity, Equation (1) from Temi et al. (2009) predicts a $K_S$-band luminosity of $L_{K_S}/L_{K,\odot} = 1 \times 10^{12}$. Using 2MASS $K_S$-band data, assuming a solar $H$-band magnitude of 3.32 mag (Binney & Merrifield 1998), $(B - V) = 0.97$ (de Vaucouleurs et al. 1991), and a distance of 16.5 Mpc, we measured within the same area an integrated $L_{K_S}/L_{K,\odot} = 3 \times 10^{11}$, i.e., a factor of $\sim 3$ difference from the predicted $L_{K_S}/L_{K,\odot}$, but still within the rms of

Equation (1) from Temi et al. (2009). This is consistent with the hypothesis that the FIR emission may originate from an old stellar population. It is also in agreement with the fact that the observed FIR profile is flatter than the FUV profile (see the upper-right panel of Figure 9).

### B.2. Star Formation Activity in NGC 4647

The FIR and UV emission from late-type galaxies has a substantially different origin from the corresponding emission from early-type galaxies. The UV photons are irradiated from the photospheres of young, massive O and B stars, which are embedded in molecular clouds. As the latter are usually dust rich, the dust grains are heated by absorbing the ionizing photons and emiting FIR radiation. Both FIR and UV emission from spiral galaxies is distributed along the disk, tracing the location of the spiral arms and the star formation activity of the galaxy.

The spiral galaxy NGC 4647 appears to be approximately $2'.5$ away from the elliptical NGC 4649. Due to their proximity, it is difficult to disentangle their X-ray populations. NGC 4647 should be dominated by short-lived ($< 10$–50 Myr, $M_{opt} > 5\,M_\odot$) high-mass X-ray binaries (HMXBs), in contrast with the long-lived ($> 1$ Gyr, $M_{opt} < 1\,M_\odot$) LMXB population hosted by the elliptical galaxy NGC 4649. The number of HMXBs in late-type galaxies is proportional to the star formation rate (SFR) of the host galaxy (Grimm et al. 2003; Mineo et al. 2012). In order to estimate the predicted number of HMXBs in NGC 4647, we used the calibration from Mineo et al. (2012). Accordingly, we calculated the integrated SFR inside the $D25$ ellipse of NGC 4647 using the combined NUV and FIR proxy from Iglesias-Páramo et al. (2006):

$$\mathrm{SFR}(M_\odot\,\mathrm{yr}^{-1}) = \mathrm{SFR}_{\mathrm{NUV},0} + \mathrm{SFR}_{\mathrm{IR}}. \qquad \mathrm{(B1)}$$

The first term in Equation (A1) is proportional to the NUV luminosity uncorrected for dust attenuation, taking into account the UV light from young stars escaping the dust clouds. The second term is instead based on the 8–1000 $\mu$m luminosity, tracing the emission from dust surrounding the young stars (see Mineo et al. 2012, and references therein for details about the conversion from $24\,\mu$m into 8–1000 $\mu$m luminosity.). The integrated SFR within the $D25$ ellipse of the spiral galaxy NGC 4647 is $\sim 2.7\,M_\odot$ yr$^{-1}$. In the same region, Luo et al. (2013) detected 53 X-ray sources with luminosities greater than $9 \times 10^{36}$ erg s$^{-1}$. Of these sources, 49 are in the field and four are associated with GCs. Based on the $N_X$–SFR in Mineo et al. (2012, their Equation (20)), the expected number of HMXBs in NGC 4647 with luminosities above the same threshold limit is $N_X(L > 9 \times 10^{36}$ erg s$^{-1}) \sim 37$. Taking into account an accuracy of rms = 0.34 dex on this prediction and considering that an unknown fraction of the 53 X-ray sources located within the $D25$ of NGC 4647 are LMXBs hosted by NGC 4646, the expected number of HMXBs in NGC 4647 is consistent with the observed number of X-ray binaries located within its $D25$. Therefore, in the following analysis we disregard the data within the $D25$ of NGC 4647.

To further investigate the star formation activity of the spiral galaxy NGC 4647 and its relation with the host X-ray binary population, we obtained the spatially resolved map of SFR surface density, which is displayed in Figure 10. This map was constructed from *Spitzer* and *GALEX* archival data, following the prescription by Leroy et al. (2008, their Equation (D11)):

$$\Sigma_{\mathrm{SFR}} = 8.1 \times 10^{-2} I_{\mathrm{FUV}} + 3.2 \times 10^{-3} I_{24\,\mu m}. \qquad \mathrm{(B2)}$$

---

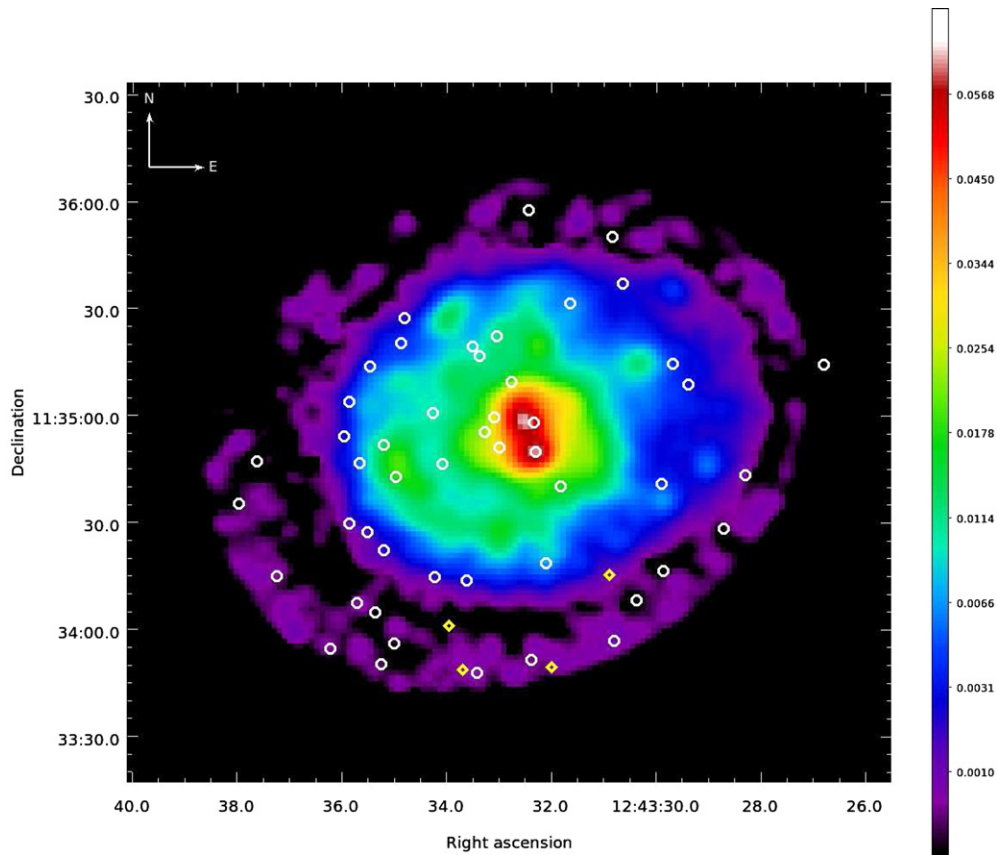**Figure 10.** SFR density image for NGC 4647, in units of $M_\odot$ yr$^{-1}$ kpc$^{-2}$, obtained by combining *GALEX* FUV and *Spitzer* 24 $\mu$m images according the prescription of Leroy et al. (2008). See Appendix B.2 and Mineo et al. (2013) for details on how the image was obtained. A slight smoothing was applied to the image, using a Gaussian kernel. The white circles and the yellow diamonds mark the locations of field LMXBs and GC-associated LMXBs, respectively, detected within the *D*25 ellipse of NGC 4647.

(A color version of this figure is available in the online journal.)

$I_{\rm FUV}$ and $I_{24\,\mu m}$ are in units of MJy sr$^{-1}$. To combine the FUV and 24 $\mu$m images, which have reasonably similar angular resolutions (4″ and 6″ FWHM, respectively) and sensitivities, we followed Mineo et al. (2013), using the same tools as for obtaining the stellar mass map (see Appendix A for details). After having spatially interpolated the 24 $\mu$m image in order to match the better resolution of the FUV image, we combined the two images and obtained the SFR density map for NGC 4647, in units of $M_\odot$ yr$^{-1}$ kpc$^{-2}$. From Figure 10, it is evident that most of the 53 X-ray sources detected within the *D*25 of NGC 4647 are located along the spiral arms of the host galaxy, confirming that they are actually dominated by HMXBs.

## REFERENCES

Bell, E. F., & de Jong, R. S. 2001, ApJ, 550, 212
Bellazzini, M., Pasquali, A., Federici, L., Ferraro, F. R., & Pecci, F. F. 1995, ApJ, 439, 687
Bildsten, L., & Deloye, C. J. 2004, ApJL, 607, L119
Binney, J., & Merrifield, M. 1998, in Galactic Astronomy, ed. J. Binney & M. Merrifield (Princeton, NJ: Princeton Univ. Press)
Brodie, J. P., & Strader, J. 2006, ARA&A, 44, 193
Chabrier, G. 2003, ApJL, 586, L133
Clark, G. W. 1975, ApJL, 199, L143
de Vaucouleurs, G., de Vaucouleurs, A., Corwin, H. G., et al. 1991, Third Reference Catalogue of Bright Galaxies (RC3) (New York: Springer)
Fabbiano, G. 2006, ARA&A, 44, 323
Fabbiano, G., Brassington, N. J., Lentati, L., et al. 2010, ApJ, 725, 1824
Fragos, T., Lehmer, B. D., Naoz, S., Zezas, A., & Basu-Zych, A. R. 2013a, ApJL, 776, L31
Fragos, T., Lehmer, B., Tremmel, M., et al. 2013b, ApJ, 764, 41

Georgakakis, A., Nandra, K., Laird, E. S., Aird, J., & Trichas, M. 2008, MNRAS, 388, 1205
Giacconi, R. 1974, in Proc Symp. 64, Gravitational Radiation and Gravitational Collapse (Dordrecht: Reidel), 147
Gilfanov, M. 2004, MNRAS, 349, 146
Grimm, H.-J., Gilfanov, M., & Sunyaev, R. 2003, MNRAS, 339, 793
Grindlay, J. E., Hertz, P., Steiner, J. E., Murray, S. S., & Lightman, A. P. 1984, ApJL, 282, L13
Grindlay, J. E. 1993, AdSpR, 13, 597
Hodge, P. W. 1962, PASP, 74, 248
Humphrey, P. J., & Buote, D. A. 2004, ApJ, 612, 848
Iglesias-Páramo, J., Buat, V., Takeuchi, T. T., et al. 2006, ApJS, 164, 38
Irwin, J. A. 2005, ApJ, 631, 511
Ivanova, N. 2006, ApJ, 636, 979
Ivanova, N., Heinke, C. O., Rasio, F. A., Belczynski, K., & Fregeau, J. M. 2008, MNRAS, 386, 553
Ivanova, N., Fragos, T., Kim, D.-W., et al. 2012, ApJL, 760, L24
Jordán, A., Côté, P., Ferrarese, L., et al. 2004, ApJ, 613, 279
Jordán, A., Sivakoff, G. R., McLaughlin, D. E., et al. 2007, ApJL, 671, L117
Jordán, A., Peng, E. W., Blakeslee, J. P., et al. 2009, ApJS, 180, 54
Juett, A. M. 2005, ApJL, 621, L25
Kim, D.-W., & Fabbiano, G. 2003, ApJ, 586, 826
Kim, D.-W., & Fabbiano, G. 2004, ApJ, 611, 846
Kim, E., Kim, D.-W., Fabbiano, G., et al. 2006, ApJ, 647, 276
Kim, D.-W., Fabbiano, G., Brassington, N. J., et al. 2009, ApJ, 703, 829
Kim, D.-W., Fabbiano, G., Ivanova, N., et al. 2013, ApJ, 764, 98
Kormendy, J., Fisher, D. B., Cornell, M. E., & Bender, R. 2009, ApJS, 182, 216
Kundu, A., Maccarone, T. J., & Zepf, S. E. 2002, ApJL, 574, L5
Kundu, A., Maccarone, T. J., & Zepf, S. E. 2007, ApJ, 662, 525
Lanz, L., Zezas, A., Brassington, N., et al. 2013, ApJ, 768, 90
Lee, M. G., Hwang, H. S., Park, H. S., et al. 2008, ApJ, 674, 857
Leroy, A. K., Walter, F., Brinks, E., et al. 2008, AJ, 136, 2782
Luo, B., Fabbiano, G., Fragos, T., et al. 2012, ApJ, 749, 130

Luo, B., Fabbiano, G., Strader, J., et al. 2013, ApJS, 204, 14
Maccarone, T. J., Kundu, A., & Zepf, S. E. 2004, ApJ, 606, 430
Masters, K. L., Jordán, A., Côté, P., et al. 2010, ApJ, 715, 1419
Mineo, S., Gilfanov, M., & Sunyaev, R. 2012, MNRAS, 419, 2095
Mineo, S., Rappaport, S., Steinhorn, B., et al. 2013, ApJ, 771, 133
O'Connell, R. W. 1999, ARA&A, 37, 603
Paolillo, M., Puzia, T. H., Goudfrooij, P., et al. 2011, ApJ, 736, 90
Peacock, M. B., Maccarone, T. J., Kundu, A., & Zepf, S. E. 2010, MNRAS,
    407, 2611
Peng, E. W., Jordán, A., Côté, P., et al. 2008, ApJ, 681, 197
Pineau, F.-X., Motch, C., Carrera, F., et al. 2011, A&A, 527, A126
Randall, S. W., Sarazin, C. L., & Irwin, J. A. 2004, ApJ, 600, 729
Roberts, T. P., Fabbiano, G., Luo, B., et al. 2012, ApJ, 760, 135
Sarazin, C. L., Kundu, A., Irwin, J. A., et al. 2003, ApJ, 595, 743
Sivakoff, G. R., Jordán, A., Sarazin, C. L., et al. 2007, ApJ, 660, 1246
Strader, J., Fabbiano, G., Luo, B., et al. 2012, ApJ, 760, 87
Temi, P., Brighenti, F., & Mathews, W. G. 2007, ApJ, 660, 1215
Temi, P., Brighenti, F., & Mathews, W. G. 2008, ApJ, 672, 244
Temi, P., Brighenti, F., & Mathews, W. G. 2009, ApJ, 707, 890
van den Bergh, S., Morbey, C., & Pazder, J. 1991, ApJ, 375, 594
Verbunt, F., & van den Heuvel, E. P. J. 1995, in X-Ray Binaries, ed. W. H. G.
    Lewin, J. van Paradijs, & E. P. J. van den Heuvel (Cambridge: Cambridge
    Univ. Press), 457
Verbunt, F., & Lewin, W. H. G. 2006, Compact Stellar X-ray Sources, ed. W.
    Lewin & M. van der Klis (Cambridge: Cambridge Univ. Press), 341
Voss, R., & Gilfanov, M. 2007, MNRAS, 380, 1685
Voss, R., Gilfanov, M., Sivakoff, G. R., et al. 2009, ApJ, 701, 471
White, R. E., III, Sarazin, C. L., & Kulkarni, S. R. 2002, ApJL, 571, L23
Wu, X.-B., & Jia, Z. 2010, MNRAS, 406, 1583
Zacharias, N., Monet, D. G., Levine, S. E., et al. 2004, BAAS, 36, 1418
Zhang, Z., Gilfanov, M., Voss, R., et al. 2011, A&A, 533, A33
Zhang, Z., Gilfanov, M., & Bogdan, A. 2012, A&A, 556, A9
Zhang, Z., Gilfanov, M., & Bogdán, Á. 2012, A&A, 546, A36
Zibetti, S., Charlot, S., & Rix, H.-W. 2009, MNRAS, 400, 1181